Modeling the Combustion-Deflagration-Detonation Transition (CoDDT) in a porous high explosive, comparison with experiments

Thomas Bouchet, Ashwin Chinnayya, Eric Fousson

To cite this version:

Thomas Bouchet, Ashwin Chinnayya, Eric Fousson. Modeling the Combustion-Deflagration-Detonation Transition (CoDDT) in a porous high explosive, comparison with experiments. Journal of Energetic Materials, 2024, pp.1-19. ⟨10.1080/07370652.2024.2397941⟩. ⟨hal-04710005⟩

HAL Id: hal-04710005

https://hal.science/hal-04710005v1

Submitted on 26 Sep 2024

Modeling the Combustion-Deflagration-Detonation Transition (CoDDT) in a porous high explosive, comparison with experiments

Thomas Bouchet[a,b*], Ashwin Chinnayya[a], Eric Fousson[b]

[a]*Institut Pprime, UPR 3346 CNRS, ISAE-ENSMA, Université de Poitiers, 1 av. Clément Ader, 86360 Chasseneuil du Poitou, France*

[b]*French-German Research Institute of Saint-Louis, 5 rue Général Cassagnou, 68300 Saint-Louis, France*

*Present Address: CEA Le Ripault, 37260 Monts, thomas.bouchet@cea.fr

Modeling the Combustion-Deflagration-Detonation Transition (CoDDT) in a porous high explosive, comparison with experiments

Abstract

A reactive multiphase model stemming from the Baer and Nunziato model was developed and extended to three phases, one solid and two gaseous respectively representing the solid explosive, the initial porosity and the reaction products. It was used to model the transition from deflagration to detonation of a highly confined porous HMX 150–200 explosive thermally initiated, for several initial densities, ranging from 65% to 88% of the material's Theoretical Maximum Density (TMD). The influence of the deconsolidative burning in the critical acceleration of the reactive front was implemented through a fluidization parameter, allowing to switch from pore to grain burning. Other microstructural parameters such as the pores and grains size were determined by careful experimental characterizations presented in Bouchet et al. (2022). The model then succeeded in reproducing the physical mechanisms that were previously experimentally observed, such as the convective burning, the plug formation, and the transition to detonation at the distances that were experimentally measured.

Keywords: deflagration, detonation, transition, HMX, numerical modeling

1. Introduction

The Combustion-Deflagration-Detonation Transition (CoDDT) phenomenon can be cast as a sequence of different physical and chemical mechanisms that occur in a thermally stressed energetic material. This can happen either accidentally in cases such as an ammunition stored in the vicinity of a fire or intentionally as in the case of a thermal cook-off test to evaluate the safety threshold of an energetic substance. The thermal input can be direct through a flame or a laser irradiation, or can be indirect like the heat induced by the impact of a low-velocity piston, as shown by McAfee et al. (1989). One consequence of this sequence of mechanisms, composed of conductive, convective and compression burning, is the gradual acceleration of the decomposition front of the material, finally leading to detonation. This sequence of mechanisms has been widely studied in order to understand the parameters influencing its occurrence and the pre-detonation distance.

In Bouchet et al. (2022), an experimental study was conducted in order to determine the influence of the microstructure on the CoDDT occurrence of highly confined porous HMX. Three batches differing by their initial granulometry were studied (M3c with a mean particle size of ~1 µm, Class E at ~10 µm and 150-200 at ~200 µm). Those batches were compacted in tubes at different densities and their respective microstructure before and after compaction was finely characterized through different technics: laser granulometries for particle size distribution, BET measurements for specific surface area, helium pycnometries for open porosities estimation and mercury porosimetries for pore size distribution. Those microstructural characterizations revealed that the biggest grains were highly damaged by the compaction process, up to the point that the three batches final granulometries became similar. However, the pores size distribution has been found to be significantly different for each batch and at each compaction density. Indeed, it was observed that the greater the initial granulometry, the greater the average pore size for a given density, and the greater the density, the smaller the pore size for a given batch.

Afterwards, those three batches were compacted in 80 mm long high resistance brass tubes with an inner diameter of 4 mm and a wall thickness of 2 mm or 6 mm depending on the batch studied. Those tubes were thermally ignited at one extremity with an infrared laser source, which energy was deposited using a tight opto-mechanical interface, on a small amount of HMX doped with black carbon. The dynamic deformation of the confinement was observed with a high-speed camera and short-circuit pins were placed along the tube in order to measure the pressure front velocity. Those experiments resulted in the determination of run to detonation lengths that depend on the batch initial granulometry and on the compaction density.

In parallel to the experimental work, a model was developed based on the 1-D reactive multiphase model of Baer and Nunziato (1986). The objective was to reproduce some experimental behaviors that were observed, especially the deflagration-to-detonation transition. The approach consisted in determining the influence of the measured microstructural characteristics of the compacted explosive grains and then in the calibration of the model. A report by Baer and Son (1995) summarized different approaches. Baer and Nunziato (1986) were probably the first to highlight that a two-phase reactive model was able to tackle the CoDDT process for a HMX porous material. This model considered that the velocities and temperatures of the reactive material and the products were out of equilibrium. It consisted in conservation equations for mass, momentum, and energy for each phase, as well as a porosity equation. A first approximate model was derived in the limit of infinite drag between phases (Kapila et al. (2001)), further discussed to get the Bdzil-Kapila-Stewart model (Baer and Son (1995)). A comparison between both approaches was made in a report by Baer and Son (1995). Xu and Stewart (1997) highlighted that in reactive cases, the reaction and compaction rates should be governed by different variables, and not by the same porosity variable. Following their recommendation, we proposed a three-phase modeling for CoDDT.

This paper is composed as follows. The second section is dedicated to the presentation of the model, section three shows some results with the implementation of the model for the HMX 150-200 batch compacted at 83% of the TMD, and finally the section four discusses the relevance of the obtained results.

2. A 1D multiphase reactive flow model

The following conservation equations allow the description of the modified Baer-Nunziato model that is used for reproducing the deflagration to detonation transition.

Conservation equations

$$\frac{\partial \alpha_s}{\partial t} + u_{Is}\frac{\partial \alpha_s}{\partial x} = (\mu\Delta\pi)_s + \frac{\dot{m}}{\rho_I} \tag{1}$$

$$\frac{\partial (\alpha\rho)_s}{\partial t} + \frac{\partial (\alpha\rho u)_s}{\partial x} = \dot{m} \tag{2}$$

$$\frac{\partial (\alpha\rho u)_s}{\partial t} + \frac{\partial (\alpha\rho u^2 + \alpha p)_s}{\partial x} = \pi_{Is}\frac{\partial \alpha_s}{\partial x} + F_{Ds} + \dot{m}u'_I \tag{3}$$

$$\frac{\partial (\alpha\rho E)_s}{\partial t} + \frac{\partial (\alpha\rho E u + \alpha p u)_s}{\partial x} = \pi_{Is}u_{Is}\frac{\partial \alpha_s}{\partial x} - \pi'_{Is}(\mu\Delta\pi)_s + F_{Ds}u'_I + \dot{Q}_s + \dot{m}E_I \tag{4}$$

$$\frac{\partial (\alpha\rho n)_s}{\partial t} + \frac{\partial (\alpha\rho n u)_s}{\partial x} = (\alpha\rho)_s\dot{n}_s \tag{5}$$

$$\frac{\partial \alpha_g}{\partial t} + u_{Ig}\frac{\partial \alpha_g}{\partial x} = (\mu\Delta\pi)_g \tag{6}$$

$$\frac{\partial (\alpha\rho)_g}{\partial t} + \frac{\partial (\alpha\rho u)_g}{\partial x} = 0 \tag{7}$$

$$\frac{\partial (\alpha\rho u)_g}{\partial t} + \frac{\partial (\alpha\rho u^2 + \alpha p)_g}{\partial x} = \pi_{Ig}\frac{\partial \alpha_g}{\partial x} + F_{Dg} \tag{8}$$

$$\frac{\partial (\alpha\rho E)_g}{\partial t} + \frac{\partial (\alpha\rho E u + \alpha p u)_g}{\partial x} = \pi_{Ig}u_{Ig}\frac{\partial \alpha_g}{\partial x} - \pi'_{Ig}(\mu\Delta\pi)_g + F_{Dg}u'_I + \dot{Q}_g \tag{9}$$

$$\frac{\partial (\alpha\rho n)_g}{\partial t} + \frac{\partial (\alpha\rho n u)_g}{\partial x} = (\alpha\rho)_g\dot{n}_g \tag{10}$$

$$\frac{\partial \alpha_p}{\partial t} + u_{Ip}\frac{\partial \alpha_p}{\partial x} = (\mu\Delta\pi)_p - \frac{\dot{m}}{\rho_I} \tag{11}$$

$$\frac{\partial (\alpha\rho)_p}{\partial t} + \frac{\partial (\alpha\rho u)_p}{\partial x} = -\dot{m} \tag{12}$$

$$\frac{\partial (\alpha\rho u)_p}{\partial t} + \frac{\partial (\alpha\rho u^2 + \alpha p)_p}{\partial x} = \pi_{Ip}\frac{\partial \alpha_p}{\partial x} + F_{Dp} - \dot{m}u'_I \tag{13}$$

$$\frac{\partial (\alpha\rho E)_p}{\partial t} + \frac{\partial (\alpha\rho E u + \alpha p u)_p}{\partial x} = \pi_{Ip}u_{Ip}\frac{\partial \alpha_p}{\partial x} - \pi'_{Ip}(\mu\Delta\pi)_p + F_{Dp}u'_I + \dot{Q}_p - \dot{m}E_I \tag{14}$$

$$\frac{\partial (\alpha\rho n)_p}{\partial t} + \frac{\partial (\alpha\rho n u)_p}{\partial x} = (\alpha\rho)_p\dot{n}_p \tag{15}$$

with α_k, ρ_k (kg/m^3), u_k (m/s), p_k (Pa), E_k (J/kg) being the volume fraction, density, velocity, pressure and total energy respectively. $\dot{Q}_k$ and F_{Dk} represent the heat transfer and drag force of the phase k. The three phases represented in the model are the explosive solid phase with the underscript s, the initial gaseous phase noted g, and the phase p representing the reaction products. Here, n_s is the number of grains, and n_g the number of pores. The term π_k represents the effective pressure defined as $\pi_k = p_k - \beta_k$ with β_k the granular pressure. In the following, the latter was neglected. This implies that $\pi_k = p_k$. The total energy E_k is defined as $E_k = e_k + \frac{u_k^2}{2}$. The following relations hold $\sum \alpha_k = 1$ and $\sum \dot{Q}_k = 0$. We find additional terms μ and ṁ, which are respectively the pressure relaxation coefficient and the mass flow. The fragmentation and the heat transfers were not taken into account, in the following.

Mass transfer

The mass transfer between the solid phase and the product phase was given by Vieille's law:

$$\dot{m} = A\rho_s S\left(p_g\right)^n$$

with A and n two empirical parameters. For our simulations with HMX, we used $A = 1.5 \times 10^{-9}$ m · s^{-1} · Pa^{-n} and $n = 0.9$ (Saurel et al. (2018)). The specific surface area S was defined as

$$S = 4N\pi R^2$$

The parameter S and the radius R were expressed differently depending on the volume fraction of the solid. Indeed, to model the sharp increase in combustion surface during the deconsolidative burning, a parameter α_{SW} has been incorporated to switch between combustion modes at a certain volume fraction of solid, as proposed by Massoni et al. (1999), Saurel et al. (2018). Indeed, in the beginning, the combustion is occurring at the surface of the grains. When the limit of fluidization is achieved, the combustion occurs at the surface of the pores. The parameters of the mass transfer were then defined as:

$$\begin{cases} \text{if } \alpha_s > \alpha_{SW}, N = N_g + N_p, R = R_g = \left(\dfrac{3\alpha_g}{4\pi(N_g + N_p)}\right)^{1/3} \\ \text{otherwise}, N = N_s, R = R_s = \left(\dfrac{3\alpha_s}{4\pi N_s}\right)^{1/3} \end{cases}$$

Interfacial parameters

In the model, at the interface between the solid phase and the gaseous or the product phases, the velocity was expressed as $u_I' = u_s$. In the case of a mass transfer, the interfacial density and total energy were defined as $\rho_I = \rho_s$, and $E_I = E_s$. Other more complex interfacial parameters have been derived by Saurel et al. (2018), see also Mikart (2019). However, in the limit of high ratio of gas and condensed phase acoustic impedance, which is the case of our study, the proposed limits were recovered (Chinnayya et al. (2004)).

Relaxation terms

The relaxation terms for the velocities, which have been implemented in the form of a drag force defined, for $k = g, p$, as:

$$F_{Dk} = \frac{\alpha_k \rho_k}{6(1 - \alpha_s)} C_{Dk} S(u_s - u_k)|u_s - u_k|,$$

and $F_{Ds} = -F_{Dg} - F_{Dp}$, with the drag coefficient $C_{Dk} = \frac{150\alpha_s}{Re_{pk}} + 1.75$ (Saurel et al. (2014)). The particle Reynolds number is $Re_{pk} = \alpha_k \rho_k |u_s - u_k| (2R_s)/\mu_g$, with the dynamic viscosity of the gaseous phase given by the Sutherland law (Mikart (2019)): $\mu_g = 17.16 \times 10^{-6} \left(T_g / 273\right)^{2/3}$

The pressure relaxation was modeled as: $(\mu\Delta\pi)_g = \mu_{gs}(\pi_g - \pi_s)$, $(\mu\Delta\pi)_p = \mu_{ps}(\pi_p - \pi_s)$ and $(\mu\Delta\pi)_s = -(\mu\Delta\pi)_g - (\mu\Delta\pi)_p$, $\pi'_{Ig} = \frac{\pi_g/(\rho c)_g + \pi_s/(\rho c)_s}{1/(\rho c)_g + 1/(\rho c)_s}$ and $\pi'_{Ip} = \frac{\pi_p/(\rho c)_p + \pi_s/(\rho c)_s}{1/(\rho c)_p + 1/(\rho c)_s}$, which gives $\pi_{Is}(\mu\Delta\pi)_s = -\pi'_{Ig}(\mu\Delta\pi)_g - \pi'_{Ip}(\mu\Delta\pi)_p$. The pressure relaxation coefficient depends on the grain radius:

$$\mu_{gs} = \frac{3\alpha_s\alpha_g}{2(\rho_s c_s + \rho_g c_g)R_s} \text{ and } \mu_{ps} = \frac{3\alpha_s\alpha_p}{2(\rho_s c_s + \rho_p c_p)R_s}$$

Equations of state

In order to simplify the simulations, both the solid phase and the gaseous phase have been modeled by a simple Stiffened Gas (SG) equation of state (EOS), which is defined by:

$$e = \frac{p + \gamma p_\infty}{(\gamma - 1)p} + q, \qquad p + p_\infty = \frac{\gamma - 1}{\gamma} \rho c_p T$$

The parameters are given in the Table 1 hereafter. The parameters γ and p_∞ were calibrated using the inert HMX Hugoniot (Saurel et al. (2007), Marsch (1980)).

Table 1 - Parameters of the Stiffened Gas equation of state

	ρ_0 (kg · m^{-3})	γ	p_∞ (Pa)
HMX	1903	5.5	31×10^8
Air	1	1.4	0

The products phase was modeled by Jones-Wilkins-Lee (JWL) equation of state (Baudin and Serradeill (2010), Farag and Chinnayya (2024)). The pressure and internal energy are linked through:

$$P(\nu, e) = \frac{\Gamma_p(e - e_{kp}(\nu))}{\nu} + P_{kp}(\nu)$$

with

$$e_{kp}(\nu) = \frac{A\nu_{Ref}}{R_1} e^{-R_1\left(\frac{\nu}{\nu_{Ref}}\right)} + \frac{B\nu_0}{R_2} e^{-R_2\left(\frac{\nu}{\nu_{Ref}}\right)} + \frac{k\nu_{Ref}}{\Gamma_p}\left(\frac{\nu}{\nu_{Ref}}\right)^{\Gamma_p}$$

$$e(\nu, T) = e_{kp}(\nu) + C_{vp}T, \quad P(\nu, T) = P_{kp}(\nu) + \frac{\Gamma_p C_{vp} T}{\nu}$$

$$P_{kp}(\nu) = Ae^{-R_1\left(\frac{\nu}{\nu_{Ref}}\right)} + Be^{-R_2\left(\frac{\nu}{\nu_{Ref}}\right)} + k\left(\frac{\nu_{Ref}}{\nu}\right)^{\Gamma_p+1}$$

In the Chapman-Jouguet (CJ) state, we have

$$\nu_{CJ} = \nu_{Ref} - P_{CJ}\left(\frac{\nu_{Ref}}{D_{CJ}}\right)^2, \quad k = \left(P_{CJ} - P_{ks}(\nu_{CJ}) - \frac{\Gamma_p C_{vp} T_{CJ}}{\nu_{CJ}}\right)\left(\frac{\nu_{CJ}}{\nu_{Ref}}\right)^{\Gamma_p+1}$$

The JWL parameters values are listed in the Table 2 below. The CJ parameters have been obtained using the thermochemistry code CEA SIAME (Poeuf et al. (2018)).

Table 2 - Parameters of the JWL EOS.

ν_{Ref} (m^3/kg)	5.249×10^{-4}
Γ_p	0.3
A (Pa)	7.783×10^{11}
B (Pa)	7.071×10^{9}
R_1	4.2
R_2	1.0
P_{CJ} (Pa)	39.9×10^{9}
D_{CJ} (m · s^{-1})	9272.6
T_{CJ} (K)	3777
C_{vp} (J/(kg · K))	2508

3. Simulation, Results & Discussion

Detonation velocity

With this model, we were able to simulate the acceleration of a combustion front into a detonation in a HMX mixture at different densities. The only parameter in the HMX SG EOS that has been fitted in order to reproduce the 85%TMD CJ detonation velocity was q. Only the initial porosity of the HMX was then changed. By post-processing the results, the CJ detonation velocities were obtained and validated with the velocities given by the thermochemistry codes SIAME and QUERCY.

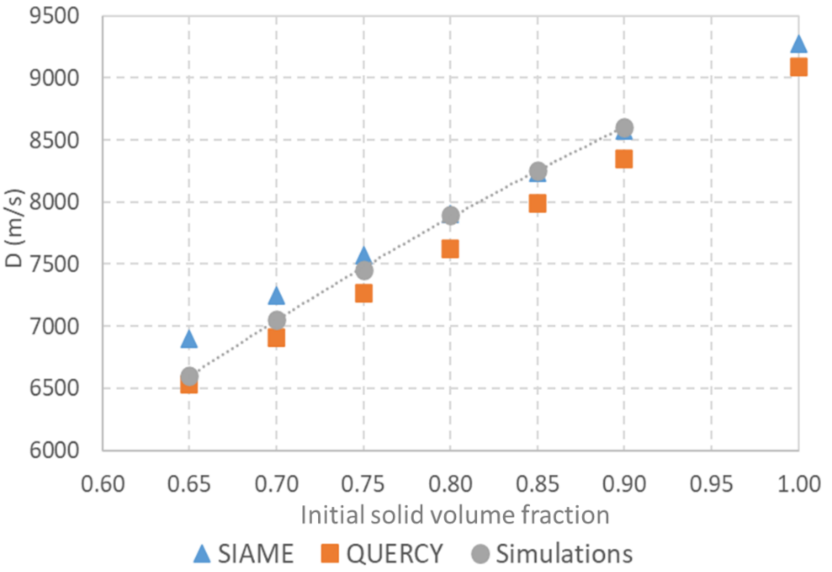

Figure 1 – Comparison of the CJ velocities between thermochemistry codes SIAME and QUERCY, and the numerical results.

What can be noted on this Figure, is that the numerical results given by our model were between QUERCY (orange squares) and SIAME (blue triangles) results. Moreover, our model accurately captured the CJ detonation velocities of SIAME for initial solid volume fractions between 0.80 and 0.90. The results were still in rather good agreement between 0.65 and 0.8.

Transition to detonation

The tests in Bouchet et al. (2022) using HMX 150-200 compacted at 83% of the TMD were chosen as a first configuration target. A long tube of this mixture initiated by a mild over-pressure chamber was simulated, as described on the Figure 2 and Table 3 hereafter. A wall boundary was imposed on the left. The mild overpressure of 1 mm mimicked the burnt gas coming from the combustion of HMX mixed with carbon, used for initiation (see experimental details in Bouchet et al. (2022)). The initial overpressure reported in Table 3 was not found to be important in the subsequent phenomena. The second zone was composed of the porous HMX. The computational domain was composed of 1001 cells, of 300 µm width. The mesh resolution was always found to be sufficient to capture the global run-up distance of CoDDT, meaning that the mesh size was chosen to be coherent with the global characteristic timescales that were modeled. Indeed, the chemical length scales were quite high for its first steps, as compared to the mesh size (see results below).

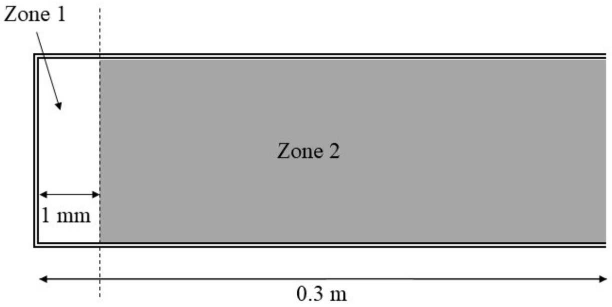

Figure 2 – Schematic of the initial conditions for the transition to detonation modeling.

Table 3 - Parameters for the modeling at 83% TMD.

	Zone 1	Zone 2
α_s	0.001	0.83
ρ_s (kg · m^{-3})	1905	1905
α_g	0.899	0.169
α_p	0.1	0.001
ρ_{g-p} (kg · m^{-3})	10	1.2
P (MPa)	15	0.1
R_s (µm)	0.625	0.625
R_g (µm)	0.45	0.45

A point to highlight is that the solid and gaseous radii, corresponding to the grain and pore sizes respectively, were obtained from the granulometry and porosimetry measurements that were performed on HMX 150-200 in Bouchet et al. (2022).

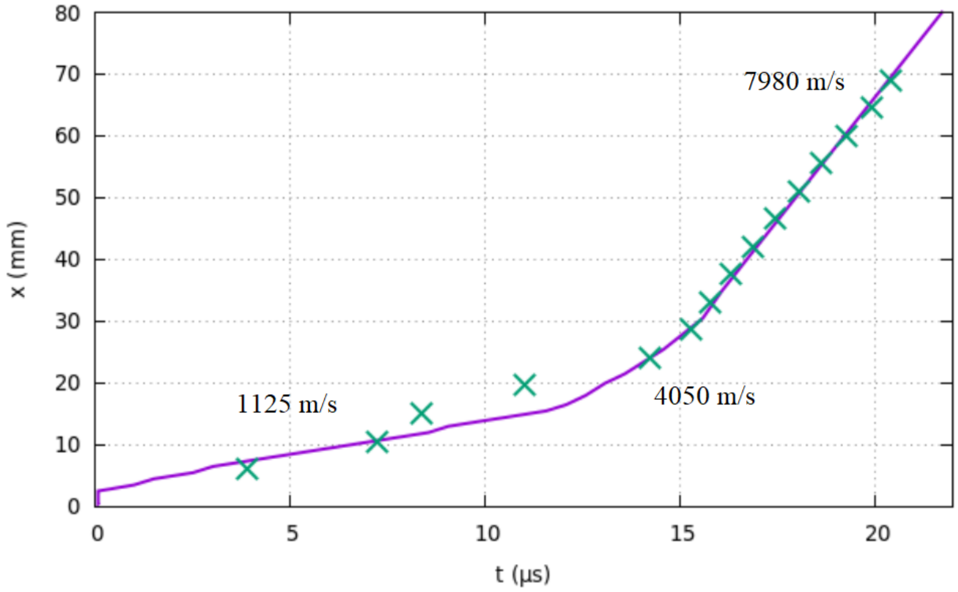

Figure 3 - Comparison of the numerical results (purple line) and the experimental data (green crosses) for the HMX 150-200 batch at 83% TMD, in the time-distance diagram.

After setting the fluidization parameter $\alpha_{SW} = 0.70$, the numerical and experimental results were compared on a time-space diagram on Figure 3. The solid line represents the results from our model and the symbols the results of short-circuit pins obtained during the CoDDT test of HMX 150-200, compacted at 83% of the TMD. A very good agreement could be observed between the experimental data and the numerical results, even though a slight temporal correction was needed due to the optical ignition process, which was not modeled.

In Figure 3, the numerical curve could be seen as composed of three distinct slopes representing, from left to right, a velocity increase. The first part has an average velocity of 1125 m/s, the second 4050 m/s and the slope of the right part an average velocity of 7980 m/s.

First thing that could be noted was that the model accurately reproduced the observed experimental detonation state, which made sense as the CJ state at 83% TMD was calibrated with the thermochemical codes. The model also reproduced accurately the location of the deflagration-to-detonation transition, which was located at 28 mm on the simulation curve. As a reminder, during the CoDDT tests in Bouchet *et al*. (2022), the transition of HMX 150-200 at 83% of the TMD was measured at approximately 27 mm.

Finally, one can observe that, even though the first four experimental points are quite dispersed, the model restituted the global velocity of this first phase.

Most of the right part represents a steady detonation, but in the first instants after the transition, a part with a slightly stiffer slope could be observed. This part represents a slight overdriven detonation due to the presence of a higher density zone right after the transition point. This phenomenon is described in Mc Afee (2010) and was also observed on our experimental data.

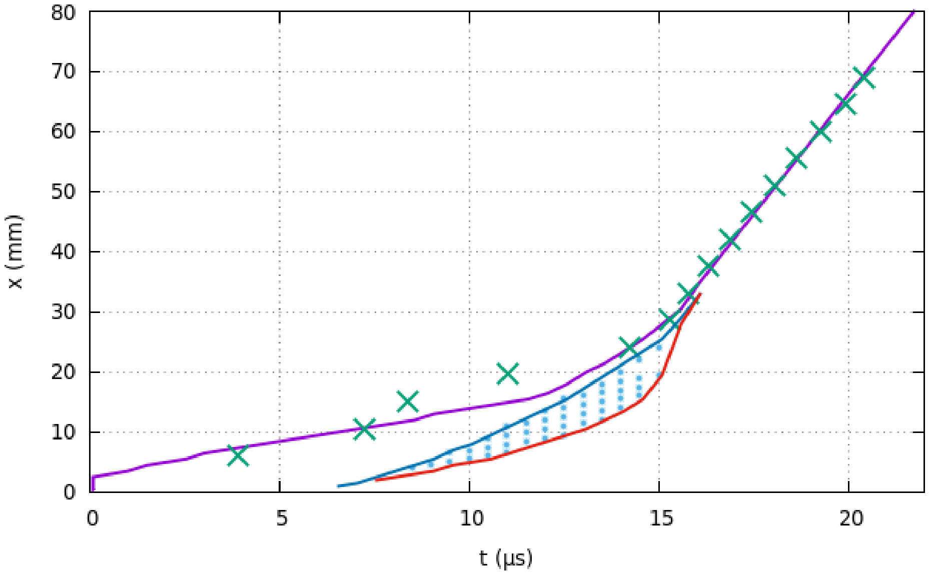

Figure 4 - Diagram (x,t) for the 83% TMD HMX, with the presence of a plug (blue dots).

Some other phenomena were also restituted by our model, as illustrated on Figure 4. The dot zone here represented the plug, reflecting the collapse of the pores under high pressure rates, and was defined by the criterion $(\alpha\rho/\rho_0)_s > 0.9$ as suggested in Parker et al. (2020). Its formation began after a few millimeters and propagated until the transition occurred. On Figure

4, the plug was delimited by two curves: the one above is an isobar of 300 MPa and the one below is an isoline defined by $(\alpha\rho/\rho_0)_s = \alpha_{SW}$.

During the first phase located in the first few millimeters, the pressure gradually increased behind the compaction wave that was traveling at 1125 m/s. The reaction rate was low and corresponded to a pore combustion mode. The solid volume fraction then decreased to a value below α_{SW} and the combustion mode changed to a grain combustion with a greater reaction rate. A deflagration front was then generated, illustrated on the Figure 4 by the red curve below the plug, along with the generation of the plug. The latter traveled at ~2000 m/s and accelerated until it reached the leading compaction wave. Both waves coalesced and a detonation wave was observed concomitantly.

Figure 5 shows the pressure profiles during the first phase, when the precursor front propagated between 8 and 13 mm, i.e. between 6.5 and 11.5 µs after initiation. The front is below 300 MPa, a value highlighted by Campbell (McAfee, 2010). A deflagration front and the associated plug were formed. The latter then caught up with the precursor compaction wave on the last profile.

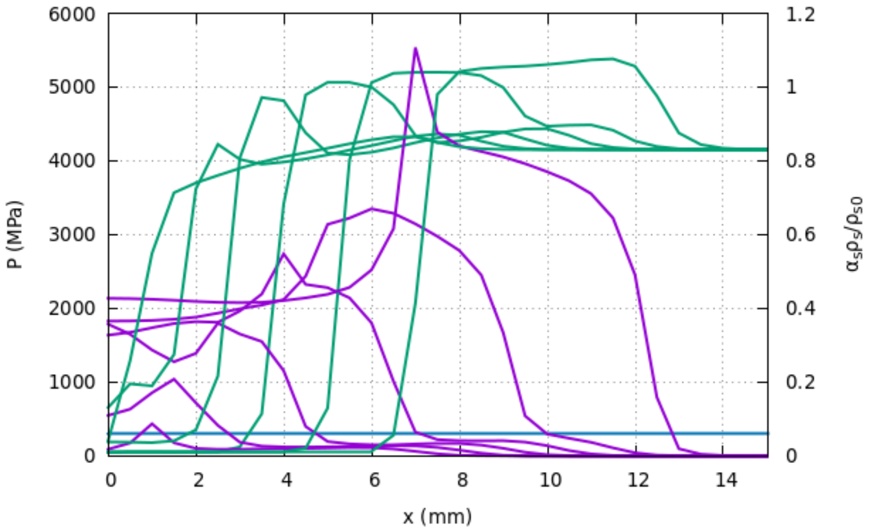

Figure 5 - Propagation of the precursor front. Profiles of pressure (purple line) and of compaction (green line) from 6.5 µs to 11.5 µs, with a 1 µs interval

Figure 6 shows the pressure profiles during the second phase. The velocity of propagation of the front face of the plug accelerates from 3600 to 4050 m/s, determined between 12 and 15.5 µs on the *x-t* diagram and using the different profiles. This is followed by a sudden acceleration towards detonation.

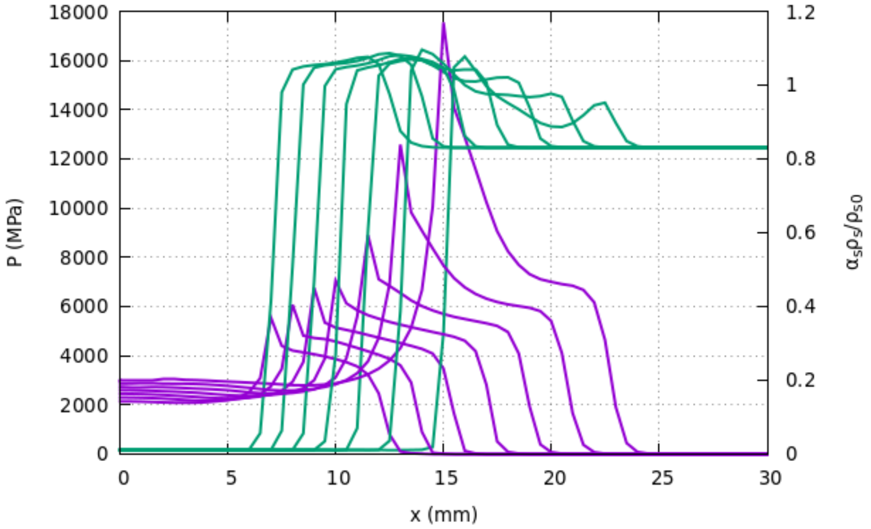

Figure 6 – Pressure (purple line) and compaction (green line) profiles of HMX 150-200 at 83% TMD from 11.5 µs to 14.5 µs, with an interval of 0.5 µs.

This model was then applied to different mixture densities in order to restitute the other CoDDT tests with the batch HMX 150-200. The grain and pore mean radii were adjusted accordingly (Bouchet et al. 2022) as well as the fluidization parameter. The results obtained can be seen hereafter in Figure 7.

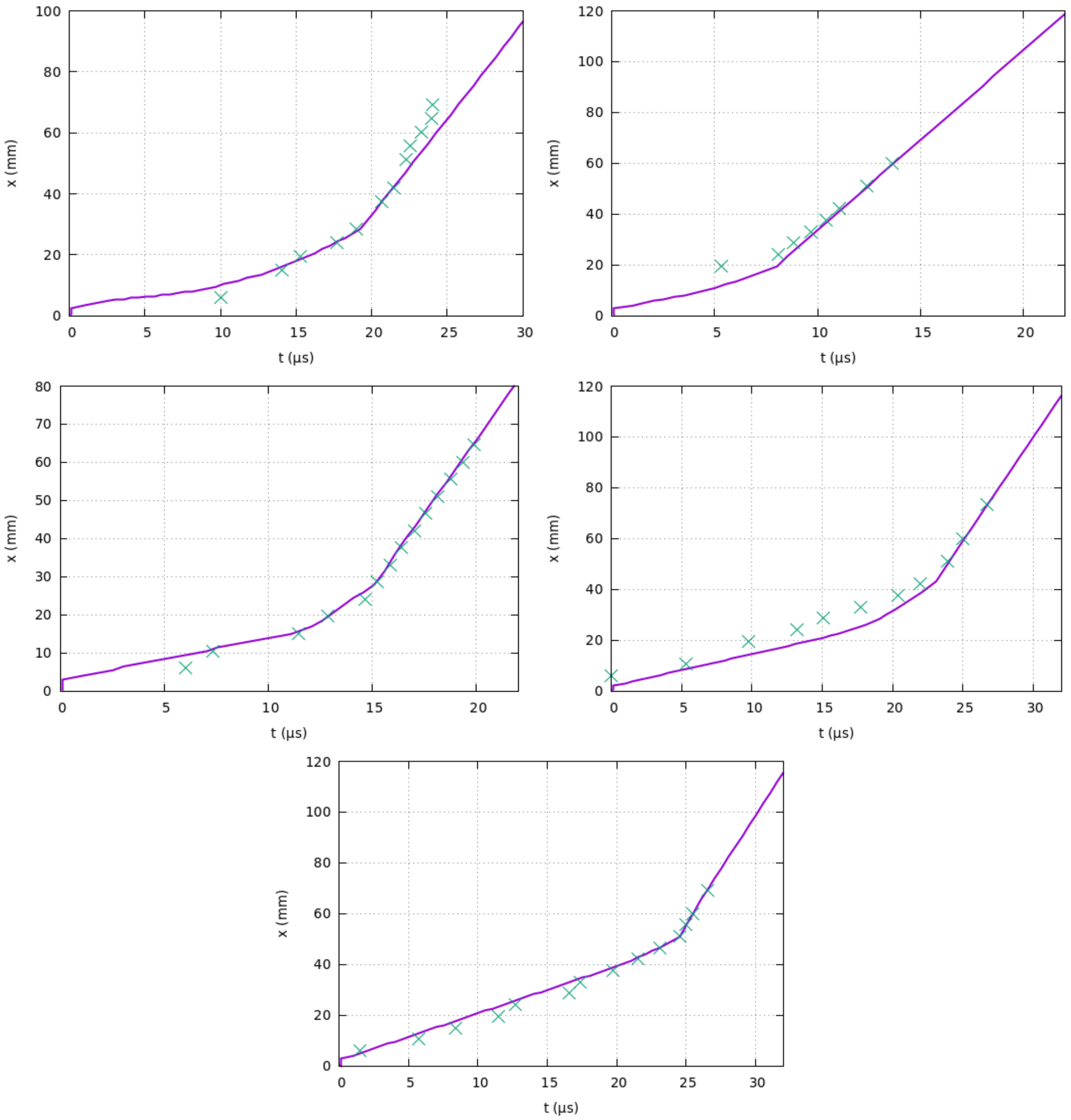

Figure 7 - Diagram (x,t) for the different density samples. 65% TMD (top left), 74% (top right), 81% (middle left), 86% (middle right), 88% (top left). Comparison between simulation results (purple solid line) versus experimental data (green crosses)

Each experimental result was reproduced with the fluidization parameter as the sole parameter, other EOS and kinetic parameters kept fixed. The radii of the grains and the pores were taken from the experiments of Bouchet et al. (2022). As for the two previous Figures 3 and 4, only a slight temporal correction was applied. Overall, the transition distances and the different velocities were accurately reproduced by our model. The following Table 4 gives the set of parameters that were used for each density and the main important results. The velocity of the phase 1 agreed well with the measurement of Griffiths and Groocock (1960) in the highest porosity case of 65%TMD.

Density (% of TMD)	DDT run (mm)(exp.)	R_{grain} (μm)	R_{pore} (μm)	DDT run (mm)(sim.)	α_{SW}	Velocity phase 1 (m/s)	Velocity phase 2 (m/s)
65	30.2	1.525	1.05	28.5	0.63	760	2250
74	22.46	1.12	0.78	19	0.75	1550	2950
81	23.12	0.85	0.60	26	0.72	1100	3700
81	22.73	0.85	0.60	26	0.72	1100	3700
81	22.44	0.85	0.60	26	0.72	1100	3700
83	26.9	0.625	0.45	28	0.7	1125	4050
83	26.97	0.625	0.45	28	0.7	1125	4050
86	42.81	0.58	0.42	44	0.66	1260	3600
88	50.43	0.40	0.30	51	0.58	1850	2800

Table 4 - Determination of the fluidization parameter for the CoDDT distance. Velocities of phases 1 and 2.

The CoDDT distance obtained experimentally and from the modeling were compared on the following Figure 8.

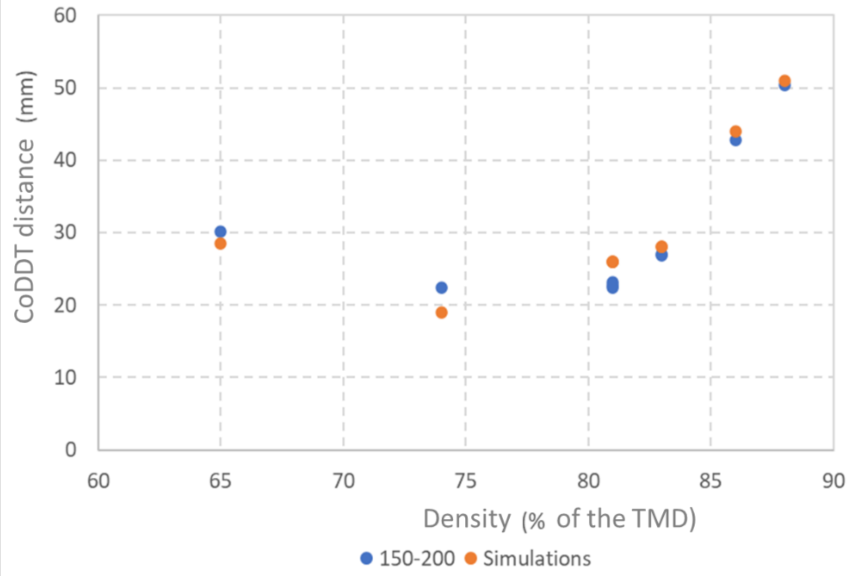

Figure 8 - Transition distances for the batch HMX 150-200, after calibration of the fluidization parameter.

We can see in the Table 4 that the value of α_{SW} decreased slightly from 0.75 to 0.7 for a density increasing from 74% to 83% of the TMD. It then dropped to 0.56 when the density increases to 88%, density at which a sharp increase of the transition distance was observed. It might be due to the higher mechanical resistance of the porous material as well as the stronger interactions between the grains and the confinement.

This variation highlighted the major role played by the deconsolidative burning, mechanism that was initially studied by Fifer and Cole (1981), and that is regularly discussed by Parker et al. (2018) (2020).

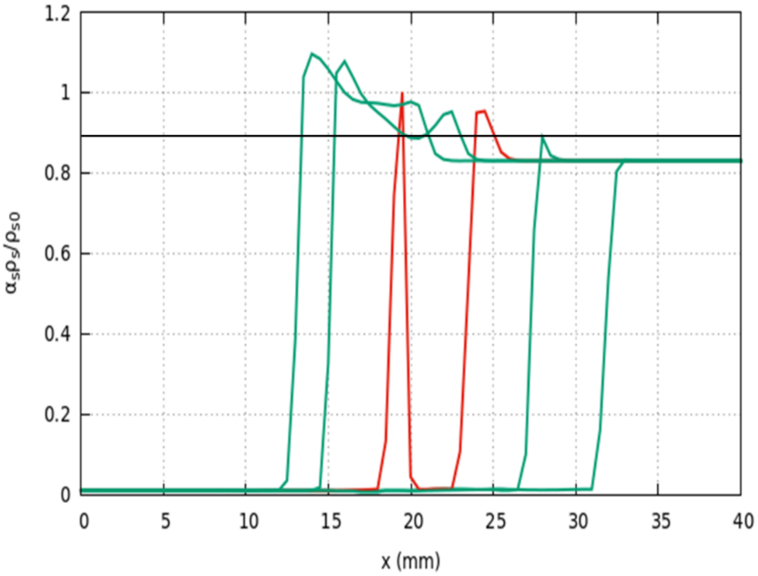

Figure 9 - Compaction profiles, at the moment of the transition, 83% TMD HMX, from 14 μs to 16 μs, with an interval of 0.5 μs. The red profile represents the moment at 15 μs when the detonation occurs in the plug

Several other phenomena observed experimentally were also restituted by our model. For example, on the Figure 9 are plotted the solid compaction rate profiles when the transition occurred (between 14 µs and 16 µs). Recall that the criterion for the plug formation was defined as $(\alpha\rho/\rho_0)_s > 0.9$. The plug evolution can be seen, notably at 15 µs (red profile) to be split into two parts. This is due to a secondary combustion front developing inside the plug. This phenomenon was observed experimentally in McAfee (2010) and Parker et al. (2018). The detonation transition could be seen to occur a few hundred nanoseconds later as the solid was consumed further.

Another phenomenon that was observed and that is specific to relatively high-porosity mixtures, as presented in McAfee (2010), is the occurrence of the convective combustion mechanism. The convective combustion, defined as a combustion regime where non-reacted solid is heated by combustion products infiltrating the pores upstream of the reactive front, can be observed on the following Figure 10.

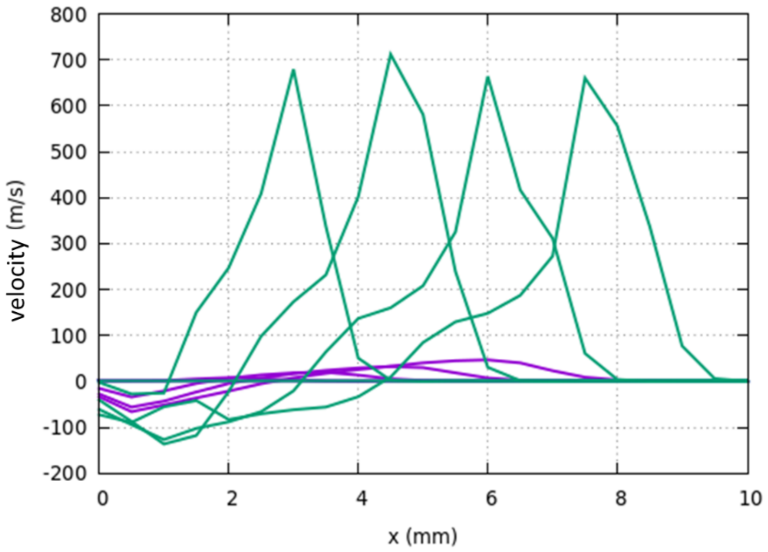

Figure 10 – Profiles of the velocities of the solid phase (purple) and the gaseous phases (green), from 0 to 6 μs, with an interval of 1.5 μs.

The solid and gas velocities were represented in purple and green, respectively. Each profile was separated by 1.5 µs. The gas velocity was much higher than that of the solid one, illustrating the intrusion of hot gases upstream of the solid velocity and combustion front, characterizing the convective burning. This mechanism was experimentally highlighted by Campbell (1980) that demonstrated the occurrence of the convective burning in the very first moments of the CoDDT in porous HMX. After these transients, no velocity disequilibrium was observed.

4. Discussions and conclusion

For this study, a reactive multiphase 1-D model inspired from Saurel et al. (2010) (2014) (2018) works, and based on a model initially developed by Baer and Nunziato (1986) was developed, which was intended to reproduce the CoDDT phenomenon.

A three-phase model, inspired by Xu and Stewart (1997) was implemented in order to differentiate between the initial porosity from that of the gaseous products. Indeed, previous models had difficulties modeling those two roles with only one gas phase. The solid, gaseous and products phases were modeled using a Stiffened Gas EOS, a perfect gas EOS and a JWL EOS, respectively. The SG EOS was fitted in order to reproduce the inert HMX polar shock. The JWL was that of HMX products. The detonation state of mixtures at different density were confronted to the CJ parameters obtained with a thermochemical code and validated, the only parameter being the initial porosity, the JWL parameters being fixed, unlike Baer and Nunziato (1986), Baer et al. (1986).

The velocity relaxation was modeled as a drag force in porous media and the mass transfer with a Vieille’s law. A fluidization parameter switched from a pore surface burning to a grain surface burning. This parameter as well as the pores and grains size were implemented using our previous experimental work (Bouchet et al. 2022).

The analysis of the numerical results of HMX at a density of 83% of the TMD enabled to decompose the transition to detonation into four main steps.

After the initiation, the reaction (pore burning) and the drag force locally increased the pressure and induced a deflagration front that propagated at a quasi-constant velocity of ~1.1-1.9 mm/µs preceded by a slight compaction front. These values were also consistent with that of Baer et al. (1986) and Bernecker and Price (1974) in other porous explosives.

Downstream of this front, the solid volume fraction then dropped under the fluidization parameter and the reaction switched to a grain surface combustion. In reality, this would correspond to the occurrence of deconsolidative burning, which may depend on the interaction of the high explosive with the confinement (Heatwole et al. (2023)), as well as on the operating condition of initial compaction before firing. This acceleration of the decomposition process and the induced deflagration wave produced strong compaction waves that propagated upstream.

After this second step, these compaction waves eventually led to a global pore collapse, resulting in the plug formation. The plug front will then accelerate and catch up the leading compaction wave. This would result in a quasi-constant velocity front (~2.8-4 mm/ µs) during this third step. Within the plug, the pressure will increase, due to chemical decomposition, along with a pressure gradient. A new reaction center site will occur within the plug, resulting into two combustion fronts, propagating at the rear and forward. During this last step, the forward combustion will catch up with the leading compaction wave, resulting eventually to the detonation onset.

Then, the fluidization parameter was calibrated in order to reproduce the CoDDT behavior of HMX at different densities between 65% and 88% of the TMD. Only this parameter needed to be calibrated, the other parameters being kept constant and the grain and pore radii taken from the measurements. This is not the case for previous models, described in the exhaustive report of Bdzil and Son (1995), in which EOS parameters needed to be redefined when the mixture porosity changed. The implementation of this fluidization parameter allowed to reproduce the brutal transition between low-speed combustion and violent deflagration preceding the detonation transition. The model was also able to recover the non-monotonic behavior of the transition distance as a function of %TMD.

Acknowledgments

The authors wish to thank Dr. Maryse Vaullerin from the CEA Gramat for the realization of the calculations with CEA SIAME needed to obtain the CJ parameters. This work pertains to the French government program "Investissements d'Avenir" (EUR INTREE, reference ANR-18-EURE-0010).

References

Baer M. and J. W. Nunziato, 1986, A two-phase mixture theory for the deflagration-to-detonation transition (DDT) in reactive granular materials. International Journal of Multiphase Flow 12 (6):861-89. DOI:10.1016/0301-9322(86)90033-9.

Baudin G. and R. Serradeill, 2010, Review of Jones-Wilkins-Lee equation of state, EPJ Web Conferences EDP Sciences, Vol. 10, p 21, DOI: 10.1051/epjconf/20101000021

Baer M. R., R. J. Gross, J. W. Nunziato and E. A. Igel, 1986, An experimental and theoretical study of deflagration-to-detonation transition (DDT) in the granular explosive, CP, Combustion and Flame 65(1), 15-30.

Bernecker, R. R. and D. Price, 1974, Studies in the transition from deflagration to detonation in granular explosives—II. Transitional characteristics and mechanisms observed in 91/9 RDX/Wax, Combustion and Flame 22(1), 119-129.

Bdzil, J.B. and S.F. Son, 1995, Engineering models of deflagration-to-detonation transition, Los Alamos National Laboratory report, LA-12794-MS

Bouchet T., E. Fousson and A. Chinnayya, 2022, Influence of the microstructure of highly confined HMX on the Combustion-Deflagration-Detonation Transition (CoDDT). Journal of Energetic Materials, DOI:10.1080/07370652.2022.2137740

Campbell A. W., 1980, Deflagration-to-detonation transition in granular HMX. Los Alamos National Laboratory report LA-UR-80-2016 United States, DOI:10.2172/5303464

Chinnayya A., E. Daniel and R. Saurel, 2004, Modelling detonation waves in heterogeneous energetic materials. Journal of Computational Physics 196(2), 490-538.

Farag G. and A. Chinnayya, 2024, On the Jones-Wilkins-Lee equation of state for high explosive products. Propellants, Explosives, Pyrotechnics, DOI: 10.1002/prep.202300223

Fifer R. A. and J. E. Cole, 1981, Transitions from laminar burning for porous crystalline explosives. Proceedings of the 7th International Symposium on Detonation, pp 164-174

Kapila A. K., R. Menikoff, J. B. Bdzil, S.F. Son, and D.S. Stewart, 2001, Two-phase modeling of deflagration-to-detonation transition in granular materials: Reduced equations, Physics of fluids, 13(10), 3002-3024.

Griffiths, N. and J. M. Groocock, 1960, The burning to detonation of solid explosives, Journal of the Chemical Society 814, 4154–4162.

Heatwole, E. M., T. A. Feagin, I. D. Lopez-Pulliam and G. R. Parker, 2023, Deflagration-to-detonation transition (DDT) in a granular high explosive in two dimensions, In AIP Conference Proceedings, Vol. 2844, No. 1, AIP Publishing.

Marsch S.P, 1980, LASL Shock Hugoniot Data, University of California Press.

Massoni J., R. Saurel, G. Baudin and G. Demol, 1999, A mechanistic model for shock initiation of solid explosives, Physics of Fluids 11(3), 710-736.

McAfee J. M., Asay B. W., Campbell A. W. and Ramsay J. B., 1991, The Deflagration-to-Detonation Transition in Granular HMX. Research Center for Energetic Materials Open Seminar on Safety and Hazards Evaluation proceedings, NM (USA)

McAfee J. M. 2010, The deflagration-to-detonation transition. In Shock wave science and technology reference library, ed. B. W. Asay, Vol. 5 (Springer), 483-536. DOI:10.1007/978-3-540-87953-4.

Mikart M., 2019, Capture, par mousse aqueuse, de particules micrométriques disperses par explosive. Étude expérimentale et numérique. PhD Thesis, ISAE-ENSMA Poitiers (France)

Parker G. R., J. Tringe, E. M. Heatwole, M. De Haven and M. Holmes, 2018, Understanding Sub-Detonative Burning and Variability in DDT Characteristics for Granular HMX Confined in Polycarbonate Tubes, 16th International Detonation Symposium

Parker G. R., E. M. Heatwole, M. D. Holmes, B. W. Asay, P. M. Dickson and J. M. McAfee, 2020, Deflagration-to-detonation transition in hot HMX and HMX-based polymer-bonded explosives. Combustion and Flame, Vol. 215, pp 295-308, DOI:10.1016/j.combustflame.2020.01.040

Poeuf S., M. Genetier, A. LeFrançois, A. Osmont, G. Baudin and A. Chinnayya, 2018, Investigation of JWL Equation of State for Detonation Products at Low Pressure with Radio Interferometry, Propellants, Explosives, Pyrotechnics, Vol. 43, pp 1157-1163, DOI:10.1002/prep.201800099

Saurel R., O. Le Métayer, J. Massoni and S. Gavrilyuk, 2007, Shock jump relations for multiphase mixtures with stiff mechanical relaxation, Shock Waves, Vol. 16, pp 209-232, DOI:10.1007/s00193-006-0065-7

Saurel R., S. Le Martelot, R. Tosello and E. Lapébie, 2014, Symmetric model of compressible granular mixtures with permeable interfaces. Physics of Fluids, Vol. 26. DOI:10.1063/1.4903259

Fraysse, D. Furfaro and E. Lapébie, 2018, Multiscale multiphase modelling of detonations in condensed energetic materials. Computers & Fluids 169: 213-29. DOI:10.1016/j.compfluid.2018.03.054.

Xu, S. and D.S. Stewart, 1997, Deflagration-to-detonation transition in porous energetic materials: a comparative model study. Journal of Engineering Mathematics 31:143-172